School of Natural Sciences and Mathematics
William B. Hanson Center for Space Sciences

Mesoscale Plasma Convection Perturbations In The High-latitude Ionosphere

UT Dallas Author(s):

Yun-Ju Chen
Roderick A. Heelis

Citation:

Chen, Y. -J, and R. A. Heelis. 2018. "Mesoscale Plasma Convection Perturbations in the High-Latitude Ionosphere." Journal of Geophysical Research: Space Physics 123: 7609-7620, doi:10.1029/2018JA025716

Journal of Geophysical Research: Space Physics

RESEARCH ARTICLE
10.1029/2018JA025716

Mesoscale Plasma Convection Perturbations in the High-Latitude Ionosphere

Yun-Ju Chen[1] and Roderick A. Heelis[1]

[1]William B. Hanson Center for Space Sciences, University of Texas at Dallas, Richardson, TX, USA

Key Points:
- Flow perturbation location and occurrence frequency are dependent on the IMF B_z and B_y
- More flow perturbations occur in regions of sunward background flow than in regions of antisunward background flow for southward IMF
- Asymmetry in the preferred direction and scale size of flow perturbations is seen in regions of sunward and antisunward background flow

Correspondence to:
Y.-J. Chen,
yxc126130@utdallas.edu

Citation:
Chen, Y.-J., & Heelis, R. A. (2018). Mesoscale plasma convection perturbations in the high-latitude ionosphere. *Journal of Geophysical Research: Space Physics*, *123*, 7609–7620. https://doi.org/10.1029/2018JA025716

Received 25 MAY 2018
Accepted 13 AUG 2018
Accepted article online 24 AUG 2018
Published online 6 SEP 2018

Abstract An investigation of flow perturbations with spatial scale sizes between 100 and 500 km in the high-latitude ionosphere is presented. These localized flow perturbations are deviations from the large-scale background convection, expected to give us new insights into the magnetosphere-ionosphere coupling process. Ion drift measurements from the Defense Meteorological Satellite Program F17 are utilized to identify these mesoscale flow perturbations. Our intent is to discover the properties of these perturbations in terms of perturbation flow speeds, location, scale size, and occurrence frequency as well as their dependence on the interplanetary magnetic field (IMF) and underlying large-scale convection pattern. Observation suggests that flow perturbation locations strongly depend on the IMF orientation as does the occurrence frequency of the flow perturbations. For southward IMF, more flow perturbations occur in regions of sunward background flow than in regions of antisunward background flow. For flow perturbations with speeds over 300 m/s, an asymmetry in the preferred direction and scale size is seen for those embedded in sunward and antisunward background flows. Significantly less asymmetry is present for flow perturbations with speeds between 100 and 300 m/s. The flow perturbations exceeding 300 m/s are most likely closed locally with lower magnitude return flows or with adjacent flows across the convection reversal boundary and representing additional sources of frictional heating and momentum transfer to the thermosphere. The perturbation flow speed is almost independent of the scale size and underlying convection speed, but the largest speeds are preferentially seen at scale sizes between 200 and 300 km.

1. Introduction

A large-scale two-cell circulation of plasma in the high-latitude ionosphere is a characteristic feature that prevails at all times during periods of southward interplanetary magnetic field (IMF; Dungey, 1961, Reiff & Burch, 1985). Studies of this convective flow from satellites and ground-based radar facilities have produced empirical models of the electrostatic potential that broadly represent the characteristics of the plasma flow and its dependence on the dominant drivers in the solar wind (Cousins & Shepherd, 2010; Ruohoniemi & Baker, 1998; Weimer, 2001). Refinements to the representation of the plasma flow from empirical models are provided through data assimilation procedures (Lu et al., 1996; Richmond & Kamide, 1988) that provide more insight into the time dependence and the spatial configuration of the convection cells. Both empirical models and data assimilation typically describe features in the ionospheric convection that have gradient-scale lengths of 500 km and above. They are used in computational models that describe the ionosphere and thermosphere (Fuller-Rowell et al., 1996; Richmond et al., 1992; Roble & Ridley, 1994) and their coupling to the magnetosphere and the solar wind at these typical scale sizes and above. In particular, these models describe the global circulation and temperature distribution of the thermosphere that result from heating by energetic particle precipitation and frictional heating with the ions. However, Codrescu et al. (1995) describe the deficiencies in these models in specifying the neutral temperature and point out that variability in the plasma flow, or equivalently the electric field, will be an important additional heat source. Following this realization, several attempts to quantify the effects of structure in the plasma velocity with small and intermediate scale between 10 and 500 km have been undertaken (Codrescu et al., 2000; Cousins & Shepherd, 2012; Crowley & Hackert, 2001; Johnson & Heelis, 2005; Kivanç & Heelis, 1998; Matsuo et al., 2003) and have led to the generation of models to describe this additional energy source to the ionosphere and thermosphere (Cosgrove & Codrescu, 2009; Matsuo & Richmond, 2008), which may be accounted for in terms of an additional heating rate.

At scale sizes less than 500 km, there exist coherent flow structures that deliver both energy and momentum to the neutral atmosphere in a manner that is not adequately described by a parameterized heating rate

(Deng & Ridley, 2007; Deng et al., 2009). Models of the high-latitude convection pattern, cited above utilizing harmonic functions, do not typically allow for a significant spatial variation in the flows across the auroral zone. Thus, these intermediate-scale size features may exist as systematic properties of the large-scale flow pattern in addition to isolated flow features that may be superimposed upon the larger scales. Such flow features have previously been identified in the cusp region and related to the signatures of sporadic merging events at the dayside magnetopause (Milan et al., 2000; Pinnock et al., 1993; Shepherd et al., 2003). So-called flow bursts have also been observed across the nightside associated with intensifications of emissions at the poleward boundary of the aurora and the onset of auroral substorms (Lyons et al., 2011; Wild & Yeoman, 2000; Zou et al., 2014). The distribution of these events is also reported by Gabrielse et al. (2018) from the systematic examination of data from the Super Dual Auroral Radar Network radars.

In this work we describe the nature of flow features in the high-latitude convection pattern with scale sizes between 100 and 500 km. Our intent here is to discover the properties of these features in terms of the magnitude, location in magnetic latitude and magnetic local time, scale size and occurrence frequency of these flow features, and their dependence on the properties of the large-scale convection pattern and the orientation of the IMF.

2. Observations

In this investigation we utilize observations from the Defense Meteorological Satellite Program (DMSP) F17 satellite that has an approximately Sun-synchronous orbit at an altitude near 840 km with an orbital plane approximately in the dawn-dusk meridian. The satellite orbital period of about 100 min provides 14–15 orbits a day. The offset of the magnetic pole and the geographic pole produces a sampling in magnetic latitude and magnetic local time that almost covers the entire auroral zone and polar cap if both the Northern and Southern Hemispheres are considered. The Special Sensor for Ions Electrons and Scintillation provides measurements of the plasma velocity, which is in the direction perpendicular to the satellite track, with a cadence of 1 s, thus describing spatial structures of scale sizes greater than 20 km. In order to obtain a high fidelity signal that is not compromised by low plasma density, the time period covers only local summer months of May to August 2012 in the Northern Hemisphere and November, December, January, and February 2012 in the Southern Hemisphere to ensure that the dayside region where plasma enters the polar cap remains in sunlight.

The 1-min average IMF measurements are used in this study and are available via the Space Physics Data Facility OMNIWeb interface. The IMF data are shifted by 10 min to account for propagation from the Earth's bow shock to the high-latitude ionosphere (Hairston & Heelis, 1995; Ridley et al., 1998; Yu & Ridley, 2009).

3. Approach

An example pass of the DMSP F17 satellite almost parallel to the dawn-dusk meridian in the northern summer hemisphere during a time of southward IMF is shown in Figure 1. It takes about 20 min for the satellite to traverse the high-latitude region and produce a signature of the convection pattern. While the entire convection pattern can change within this time, we assume that the satellite encounters stationary structures on timescales less than 2 min. This allows a simple conversion between the time series data obtained by the instrument and the spatial scale size utilizing the satellite velocity of 7.8 km/s. For the purposes of describing the background flow itself a linear adjustment to a baseline is made to ensure that the sunward flow observed at 50° magnetic latitude on both dawnside and duskside is about zero (Chen & Heelis, 2018, and the references therein). This procedure, which reflects the average behavior of the convection pattern, does not change the following characterization of plasma flow structures.

To extract plasma flow structures in the underlying large-scale convection pattern, we first identify a signature in the measured cross-track ion drift by attenuating all features with scale sizes less than 600 km utilizing an 81-point boxcar average filter (black curve in the top panel of Figure 1). Regions of positive velocity in the black curve are indicative of sunward flow at low latitudes, while regions of negative velocity indicate the antisunward flow at high latitudes, which is consistent with a typical two-cell convection pattern. A boundary that separates the sunward flow from the antisunward flow is often called the convection reversal boundary (Chen et al., 2015, 2016). Focusing on flow structures with the spatial size larger than the spatial size resolved by the sample cadence (1 Hz) of the instrument (~20 km), we also apply a low-pass seven-point boxcar

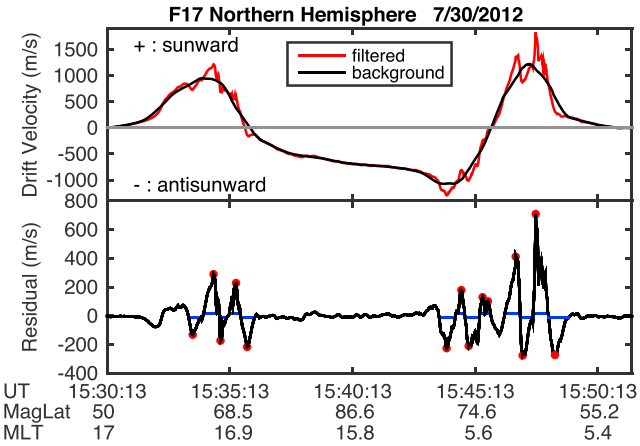

Figure 1. A pass of F17 satellite across the high-latitude regions in the Northern Hemisphere. (top panel) Red curve indicates the filtered signal that flow structures with scales less than 50 km are removed, and black curve indicates large-scale background convection velocity. (bottom panel) Residual velocity is the difference between the black and red curve in the top panel and represents the flow structure with scales between 50 and 600 km superimposed on the background convective flow. Spatial scale sizes (horizontal blue lines) and the magnitudes (red dots) of the flow perturbation are shown in the bottom panel.

average filter to remove the structures with scale sizes less than 50 km. This small-scale filtered signal with scales less than 50 km removed (red curve in the top panel of Figure 1) reveals that the plasma structures of varying amplitude superimposed on the large-scale background. Deviations from the large-scale baseline are obtained by subtracting the small-scale filtered ion drift measurement (red curve) from the large-scale convective flow signature (black curve). This residual velocity (black curve in the bottom panel of Figure 1) shows the flow structures with scale sizes between 50 and 600 km. We then identify the flow features with scale size between 100 and 500 km from this residual velocity.

Note that we identify coherent features, which are called flow perturbations in this study, as deviations in the plasma drift that both depart from and return to the baseline, rather than characterize the structure in terms of a spatial variability. For this purpose, we define a threshold near the sensitivity limit of the instrument (15 m/s) beyond which velocity perturbations are considered as flow perturbations. The distance between consecutive excursions both above and below the threshold (horizontal blue lines in the bottom panel of Figure 1) and the extremum in the velocity between the excursions (red dots in the bottom panel of Figure 1) are defined as the spatial size and the speed, respectively, of each so-called flow perturbation. This allows some perturbations to have multiple extrema as seen in the event near 15:48 UT. As described above, we further use the satellite speed (7.8 km/s) to calculate the spatial scale size from the horizontal distance in time of each perturbations and only include the flow perturbations with scales size between 100 and 500 km. We also select only flow perturbations that have the extremum shown both in the small-scale filtered signal and the residual to ensure the local extrema in the flow perturbations are not due to the difference between the gradient in the large-scale background and small-scale filtered signal.

4. Results

To describe the properties of the flow perturbations identified using the methodology above, we examine ~1,800 satellite passes in each summer hemisphere in 2012. Figure 2 shows the perturbation flow speed as a function of spatial scale (left column), the numbers of the perturbations distributed by spatial scale size (middle column) and flow speed (right column). Positive flows are directed sunward (blue) with respect to the background, and negative flows are directed antisunward (red) with respect to the background. The top panels refer to those perturbations observed on the dayside of the dawn-dusk magnetic meridian, and the bottom panels refer to those perturbations observed on the nightside of the dawn-dusk magnetic meridian. This local time division broadly separates observations taken in the Northern and Southern Hemispheres, respectively, and discussed in more detail in Figure 3. However, it indicates that little distinction can be made based on the relatively small range of solar zenith angles that are present in the observations. More perturbations are seen on the dayside than the nightside, and the majority of perturbations are seen at scale sizes between 100 and 400 km. The perturbations with scale size less than 500 km represent subgrid scale variations in typical ionosphere-thermosphere models that would be accounted for in parameterizations of the frictional heating rate described by Matsuo and Richmond (2008). The largest population of flow perturbations occurs with speeds less than 200 m/s. They represent very small deviations in the large-scale flow and are less important contributors of momentum and energy to the ionosphere and thermosphere than those features with larger magnitudes. At scales sizes between 100 and 500 km many flow perturbations are seen to exceed 300 m/s and represent coherent momentum and energy transfer features to the neutral thermosphere that should be considered in addition to the large-scale convection pattern in which they are embedded (Deng & Ridley, 2007).

Thus, we first consider the location of the flow perturbations exceeding 300 m/s at scale sizes between 100 and 500 km as a function of magnetic latitude and magnetic local time and as a function of the direction of

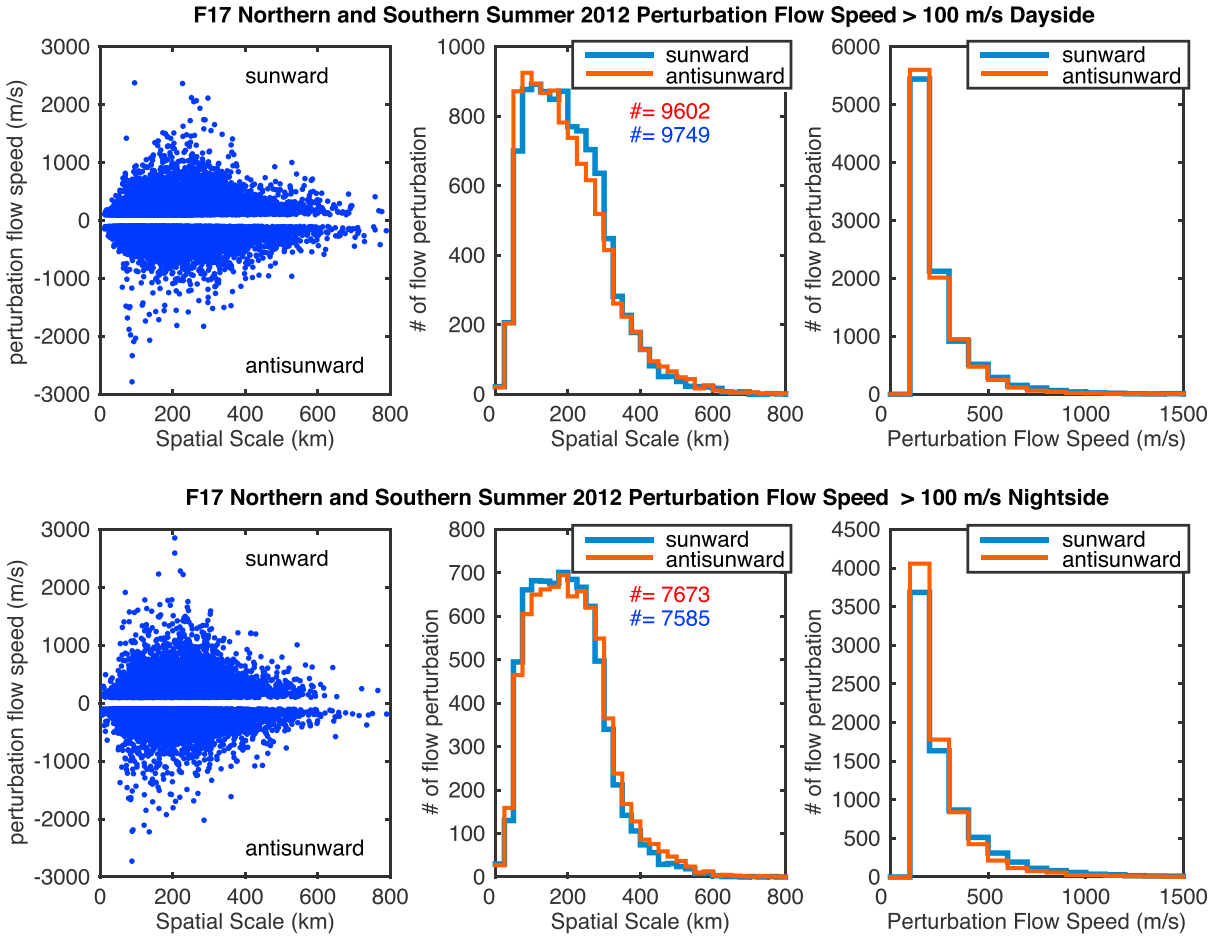

Figure 2. Perturbation flow speed as a function of spatial scale (left column), histogram of spatial scale (middle column), and histogram of perturbation flow speed (right column) for flow perturbation with magnitude larger than 100 m/s. Top row shows the observation taken from the dayside of the dawn-dusk meridian, and bottom row shows the observation taken from the nightside of the dawn-dusk meridian. In the right two columns, blue indicates the sunward directed perturbation and red indicates the antisunward directed perturbation with respect to the background.

the IMF B_z component. Figure 3 shows the distribution of these flow perturbations in magnetic latitude and magnetic local time in the Northern (left column) and Southern Hemispheres (right column) and for southward (top row) and northward IMF (bottom row). The observations are made on the dayside of the dawn-dusk magnetic meridian in the Northern Hemisphere (left column), and most of the observations in the Southern Hemisphere (right column) are made on the nightside of the dawn-dusk magnetic meridian. Red indicates antisunward directed perturbations, and blue indicates sunward directed perturbations with respect to the background. For southward IMF, flow perturbations are largely absent in the regions above 80° magnetic latitude and appear in a region that extends to 60° magnetic latitude. By contrast, during periods of northward IMF, flow perturbations migrate to higher latitudes and tend to fill in the region above 80° magnetic latitude.

To further pursue the description of flow perturbations, we restrict our attention to those seen during southward IMF when the flow perturbations are embedded in a well-recognized large-scale two-cell convection pattern as shown in the top panel of Figure 1. Figure 4 shows the distribution of these flow perturbations separated by the background flows in which they are embedded: sunward, identified as the region poleward of the convection reversal boundary (top panels) and antisunward, identified as the region equatorward of the convection reversal boundary (bottom panels). From left to right in each case are shown the distribution of background flows as a function of local time, the number of flow perturbations observed in 2-hr local time bins, the median background flow associated with each flow perturbation in each local time bin, and the location of each flow perturbation in magnetic local time and magnetic latitude. Positive background

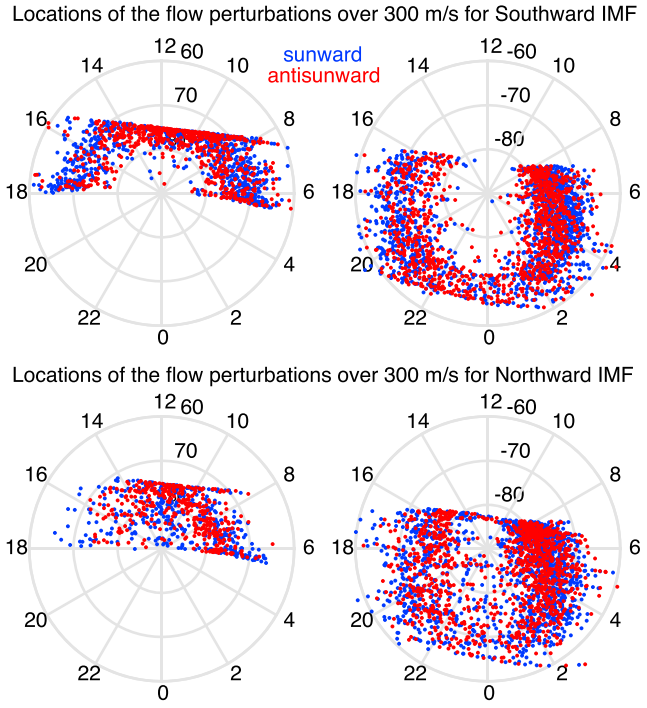

Figure 3. Location of the flow perturbations with magnitude exceeding 300 m/s at scales between 100 and 500 km in magnetic coordinate for southward IMF (top row) and northward IMF (bottom row) in Northern Hemisphere (left column) and Southern Hemisphere (right column). Red indicates antisunward directed perturbations, and blue indicates sunward directed perturbations with respect to the background. IMF = interplanetary magnetic field.

flows are sunward, and negative background flows are antisunward. As before, blue denotes those parameters for flow perturbations that are sunward and red denotes those parameters for flow perturbation that are antisunward.

The dominance of a two-cell convection pattern is clearly seen in the left panels of Figure 4 with broad regions of sunward flow for all perturbations observed in the dawn and dusk sectors. In the regions around dawn and dusk flow perturbations embedded in the antisunward background flow are confined to slightly higher latitudes (bottom polar diagram) than flow perturbations embedded in the sunward background flow (top polar diagram). We also find that most of the flow perturbations located in the regions around 12 MLT are embedded in antisunward background flows. The same is true of flow perturbations observed across 00 MLT. This simply describes a two-cell convection pattern that has antisunward flow at higher latitude and sunward return flows at lower latitude with antisunward flows near 12 and 00 MLT. A convection reversal boundary, which separates the sunward flow from the antisunward flow, is most likely located between ~75° and 80° representing the lowest latitude of the perturbations in the bottom polar diagram and the highest latitude of the perturbations in the top polar diagram, respectively.

In the middle two columns of Figure 4, there are many more flow perturbations embedded in sunward background flow, where the median background flow is about 500 m/s (top panels), than are embedded in antisunward background flow where the median background flow is about 300 m/s (bottom panels). More flow perturbations embedded in the sunward background flow have enhanced sunward flows (blue histogram and dots in the top panels) rather than antisunward flows (red

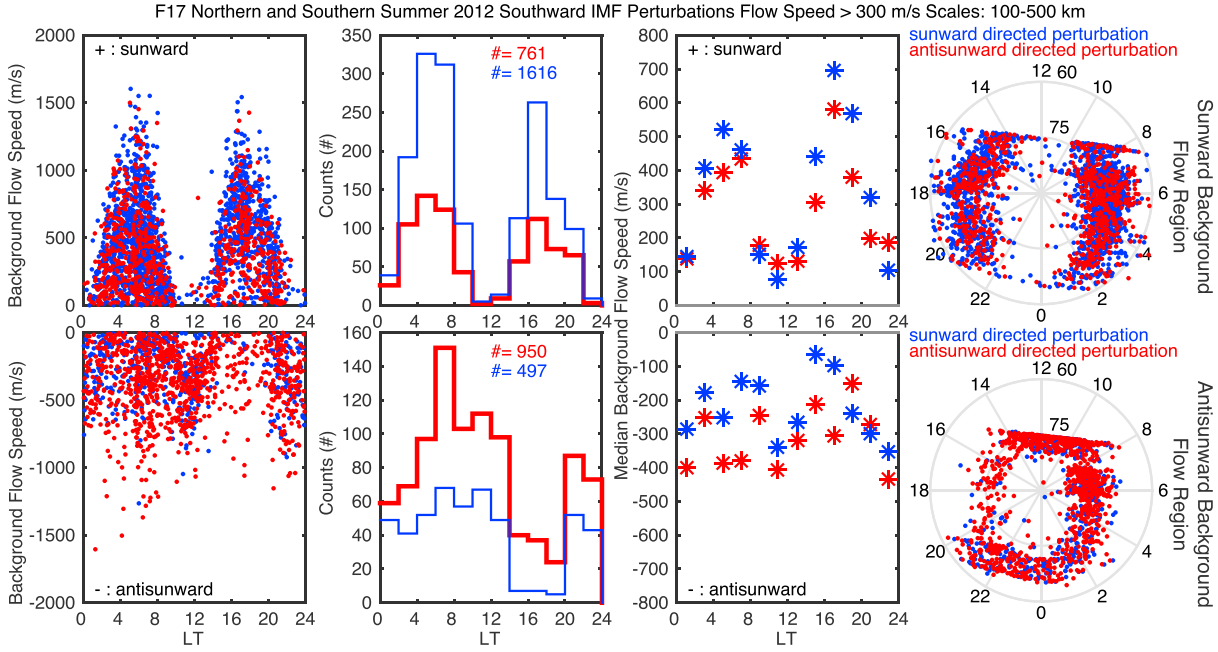

Figure 4. The distribution of background flow speed associated with flow perturbations exceeding 300 m/s as a function of magnetic local time (left column), histogram of flow perturbations (middle column), and median background flow speed in 2-hr local time bins (right column). The locations of flow perturbations in magnetic local time and magnetic latitude are shown in the right polar diagrams. Top panels refer to the flow perturbations embedded in the sunward background flows, and bottom panels refer to flow perturbations embedded in the antisunward background flows. IMF = interplanetary magnetic field.

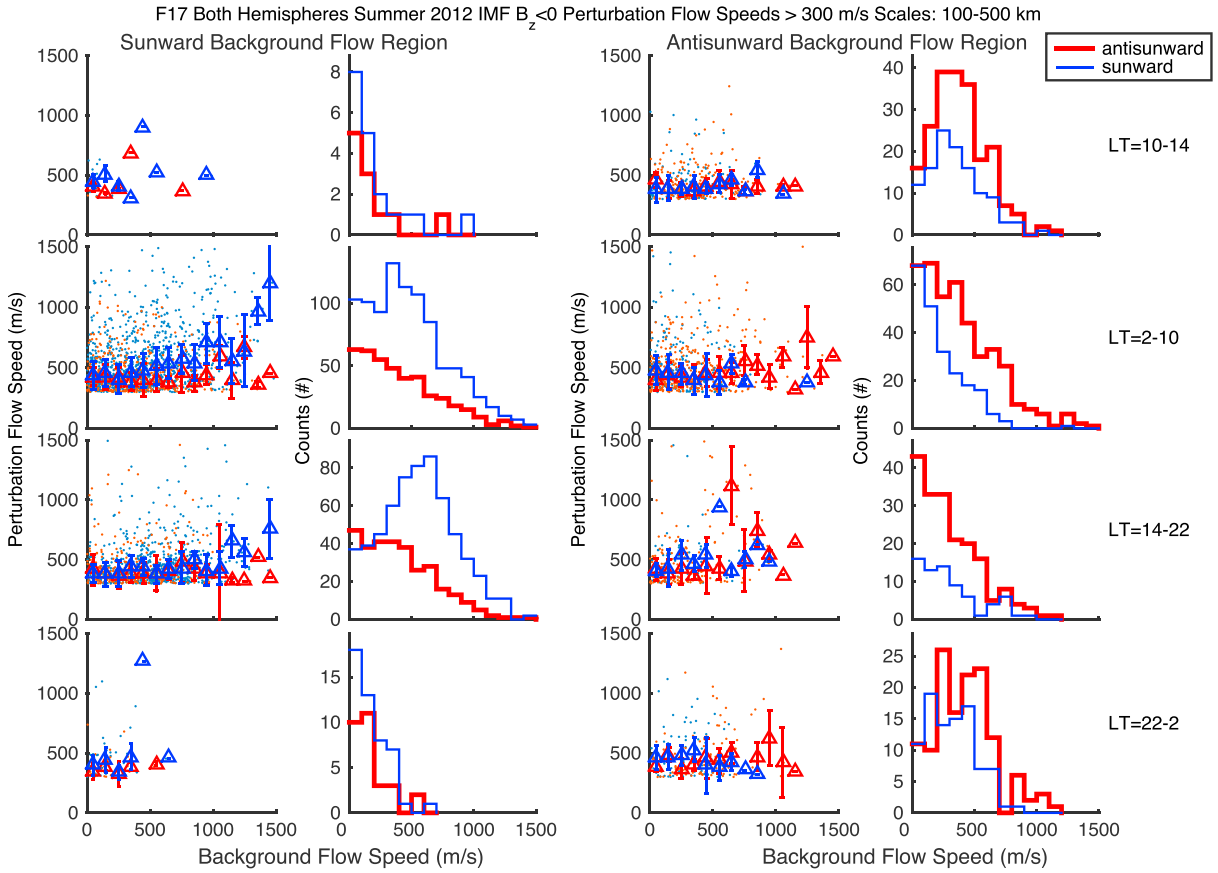

Figure 5. Perturbation flow speeds as a function of background flow speed with the medians indicated by triangles and histogram of flow perturbations in each 100-m/s background flow bins in the region of sunward background flows (left two columns) and in the region of antisunward background flows (right two columns) in four local time regions—10–14, 2–10, 14–22, and 22–2 hr (top to bottom)—for flow perturbations exceeding 300 m/s. IMF = interplanetary magnetic field.

histogram and dots in the top panels), while more perturbations embedded in the antisunward background flow have enhanced antisunward flows (red histogram and dots in the bottom panels) rather than sunward flows (blue histogram and dots in the bottom panels). We note that the histograms of flow perturbations that are embedded in the antisunward background flow (bottom panel) show an apparent preference for occurrence in the dawn sector. However, this characteristic is a sampling bias that we discuss in more detail later.

Based on the local time extent of the sunward and antisunward background flow speed as seen in Figure 4, we further group all the flow perturbations into four local time bins—10–14, 2–10, 14–22, and 22–02 hr—to study the dependence of the perturbation flow speed on the background flow as shown in Figure 5 with the sunward background cases on left and the antisunward background cases on right. Note that we have confined the local time regions across local noon and local midnight to more correctly represent the regions of reconnection on the dayside and the nightside. In the dawn and dusk sectors (second and third rows), the majority of flow perturbations are embedded in the sunward background flow (left column pair), of about 500 m/s and the majority of flow perturbations are directed sunward (blue histogram). However, the flow perturbations embedded in the antisunward background flow (right column pair) are concentrated at the convection reversal boundary, where most of the background flow speeds are much less than 500 m/s and most of the flow perturbations are directed antisunward (red histogram) in the dawn and dusk sectors (second and third rows). Most of the flow perturbations embedded in the antisunward background flows are directed antisunward across the 12 MLT (right columns and top row), while across 00 MLT (bottom row) the observed number of flow perturbations is low and a preferred direction is not pronounced.

We find that the perturbation flow speed is largely independent of the background flow except in the dawnside, where the median speed of sunward perturbations embedded in sunward background flow (blue

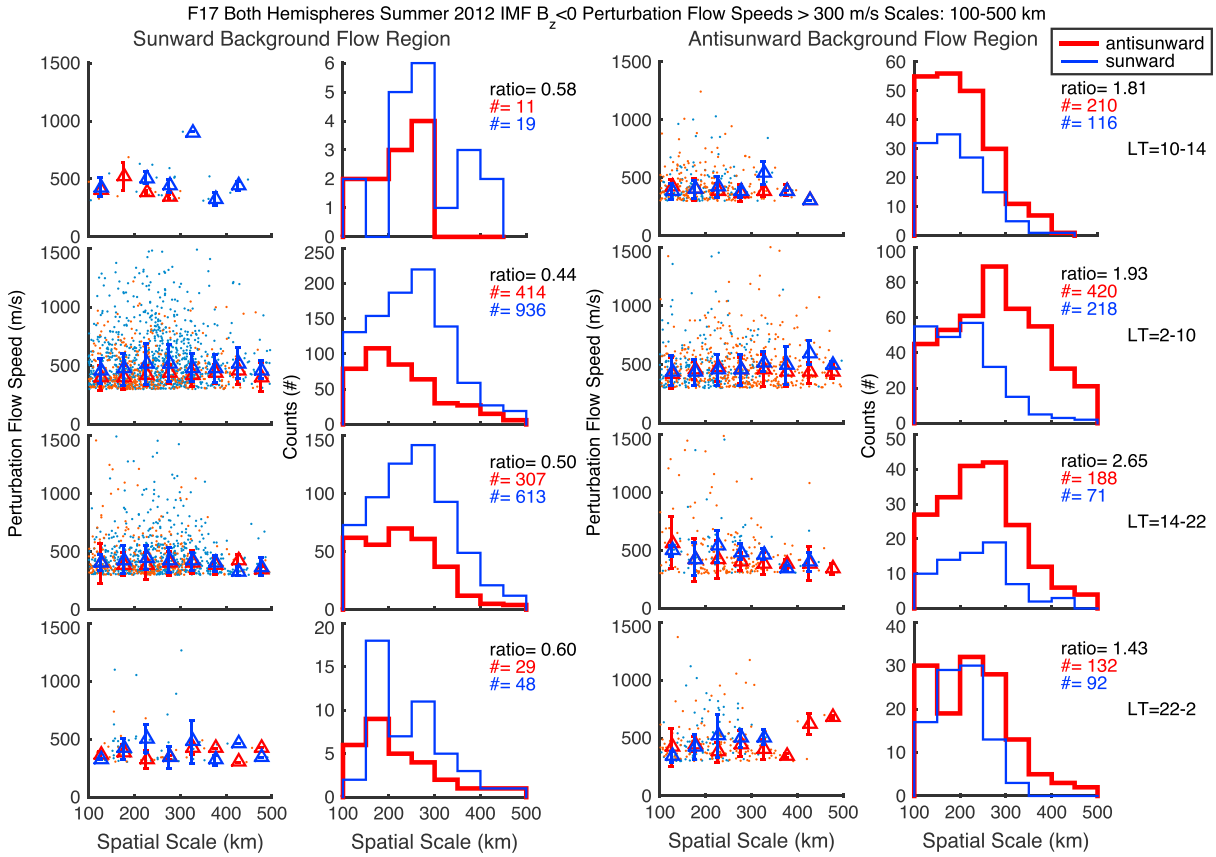

Figure 6. Perturbation flow speeds as a function of spatial scale size with the medians indicated by triangles and histogram of flow perturbations in each 100-km scale size bins in the region of sunward background flows (left two columns) and in the region of antisunward background flows (right two columns) in four local time regions (top to bottom) for flow perturbations exceeding 300 m/s. IMF = interplanetary magnetic field.

triangles, left columns, second row) increases weakly as the background flow increases. Though not illustrated here the perturbation speeds independent of typical magnetic activity parameters like Ap and AE, while the background flow itself increases with increasing magnetic activity as expected. Thus, in the presence of small background flows at the poleward and equatorward edges of the auroral zones the flow perturbations represent the dominant flow characteristics, whereas in the region with large background flow such as the heart of the auroral zone they represent reconfigurations of the large-scale flow geometry.

We further investigate the dependence of the perturbation flow speed on the spatial scale size for different local time sectors in the region of sunward background flow (left column pair) and the region of antisunward background flow (right column pair) as shown in Figure 6 in a similar format to Figure 5. While the IMF B_y component affects the location of flow perturbations, to be discussed later, it has little effect on the distribution of spatial scales for flow perturbations with speeds greater than 300 m/s in the scale size range from 100 to 500 km, and thus, we combine both positive and negative B_y observations here.

It is found immediately that the perturbation flow speed is almost independent of scale size (Figure 6), but note that as shown in Figure 2, the largest flow speeds are preferentially seen at scale sizes between 200 and 300 km. We note again that almost all flow perturbations observed across 12 MLT and across 00 MLT (top and bottom panels) are embedded in antisunward flows. The total number of sunward and antisunward directed perturbations is shown by the blue and red numbers, respectively. The ratio of antisunward to sunward directed perturbations is also shown in each local time region. The asymmetry in the preferred direction of flow perturbations in the region of sunward background flow and the region of antisunward background flow is immediately seen. In the region of sunward background flow (left column pair), sunward directed perturbations are preferred by a factor of 2 over antisunward directed perturbations. In the region of antisunward background flow (right column pair), antisunward directed perturbations are preferred over sunward directed

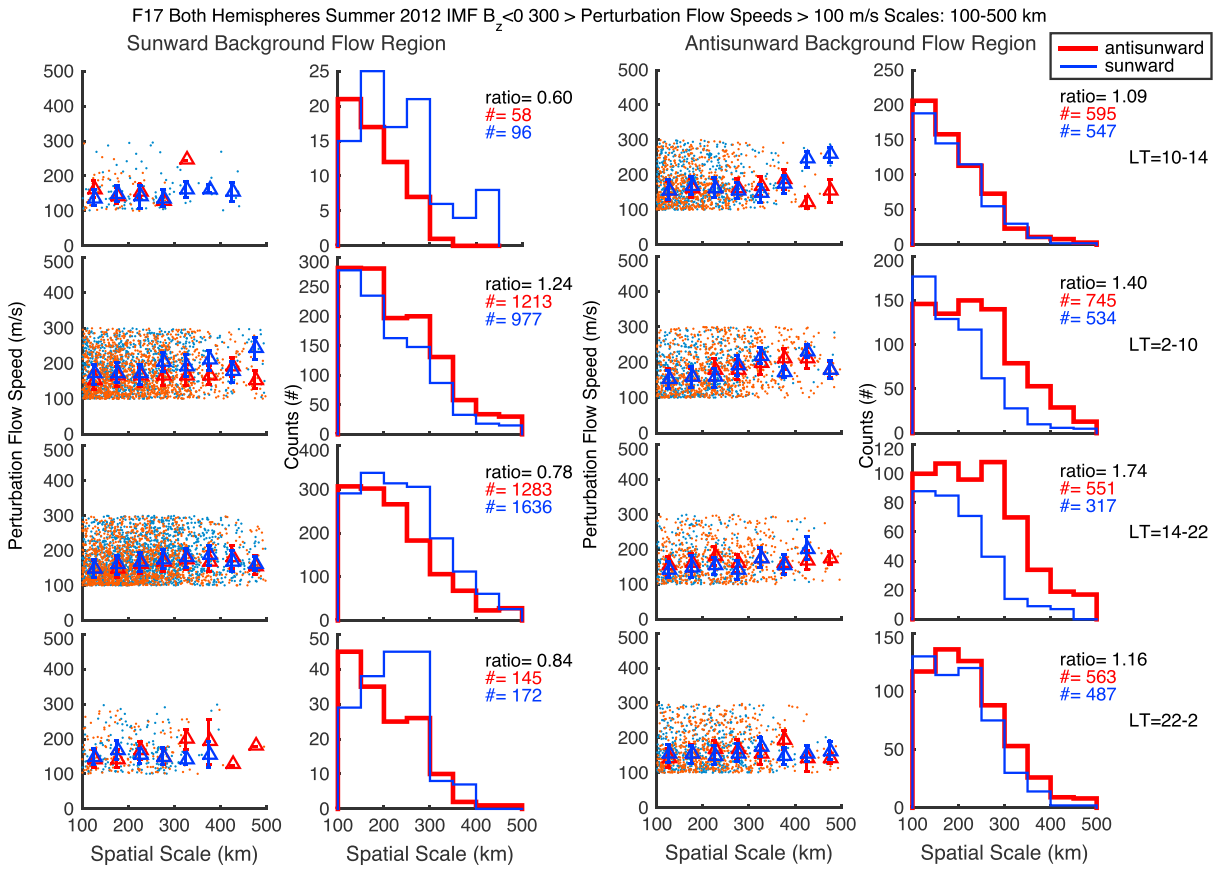

Figure 7. Perturbation flow speeds as a function of spatial scale size with the medians indicated by triangles and histogram of flow perturbations in each 100-km scale size bins in the region of sunward background flows (left two columns) and the region of antisunward background flows (right two columns) in four local time regions (top to bottom) for flow perturbations with speed between 100 and 300 m/s. IMF = interplanetary magnetic field.

perturbations by a factor of 2. It is also apparent that the preferred sunward directed flows in the region of sunward background flow (left columns) have a distribution of scale sizes that is weighted to larger spatial scales compared to the smaller number of antisunward directed perturbations. In the region of antisunward background flow (right columns), antisunward directed perturbations are preferred and in the dawnside (second row) this preferred population has a distribution of scale sizes that is weighted to larger spatial scales compared to the smaller number of sunward directed perturbations. The same preference is weakly held in the duskside where the background flow is antisunward (right columns and third row). In the 10–14 MLT sector (top panel), a preference for smaller scale sizes is present in the antisunward background region.

The systematic asymmetry in scale size and direction of perturbations is not seen in the flow perturbations with speeds less than 300 m/s. Figure 7 shows the same scale size characteristics for flow perturbations with speeds between 100 and 300 m/s in a format identical to that shown in Figure 6. As before, the perturbation flow speed is independent of spatial scale in both the sunward and antisunward background region. In the sunward background region (left column pair), the number of sunward and antisunward directed perturbations on both the dawn and dusk sides (second and third row) is about the same, as is the distribution of spatial scales. In the antisunward background region (right column pair), a preference for antisunward directed perturbations with larger spatial scales than the accompanying smaller number of sunward directed perturbations remains on both dawn and dusk sides (second and third rows), but with a smaller asymmetry than seen in the larger perturbations flow speed shown in Figure 6. Across 12 and 00 MLT (top and bottom panels), the number of sunward and antisunward directed perturbations in the antisunward background region (right columns) is about the same with the same distribution that is weighted to the smallest scale sizes. In the sunward background region (left columns), a preference for smaller-scale size is seen for antisunward directed perturbations and a preference for larger-scale size for sunward directed perturbations is present.

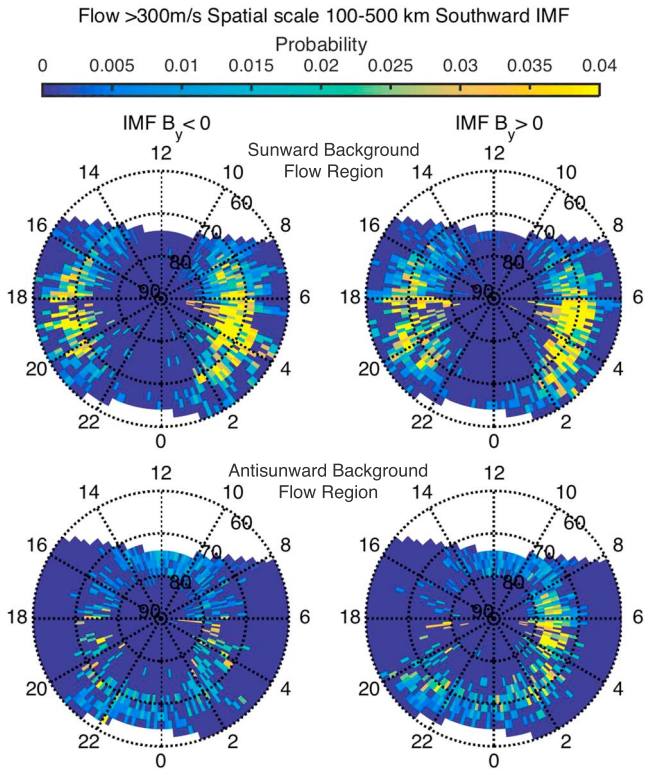

Figure 8. The occurrence probability for flow perturbations with speed greater than 300 m/s observed in the region of sunward background flows (top row) and the region of antisunward background flows (bottom row) for negative IMF B_y (left column) and positive IMF B_y (right column). IMF = interplanetary magnetic field.

Finally, we present the probability of occurrence of flow perturbations in Figure 8. Note that we find a dependence of the location of the flow perturbations on IMF B_y that is opposite in the Northern and Southern Hemispheres. Thus, we combine observations in the Northern and Southern Hemispheres using the opposite polarity in IMF B_y to recast the Southern Hemisphere observations for the equivalent Northern Hemisphere state. We divide the region into bins that are 2° by 2° in magnetic latitude and magnetic longitude, and for each bin we count the number of flow perturbations observed within it and the number of times the satellite intersects the same bin. The resulting occurrence probabilities for flow perturbations with speeds greater than 300 m/s observed in sunward background flow region (top row) and antisunward background flow region (bottom row) for positive IMF B_y on right and negative IMF B_y on left are shown in Figure 8.

In this map there is an apparent increased probability to find a flow perturbation in the dawnside in the region of sunward background flow for both polarities of B_y (top row) and in the region of antisunward background flow for positive B_y (bottom right). When B_y is negative the dawn-dusk asymmetry is less apparent in the region of antisunward background flow (bottom left) and also decreases in the region of sunward background flow (top left). We note that the dynamic range for the occurrence probability has been chosen to illustrate the spatial variations in all cases shown in Figure 8. In the dawnside regions where the occurrence frequency is saturated (top row), it may rise to 15%. It should also be emphasized that changes in IMF B_y have a dramatic effect on the orientation of the background flows, and likely the flow perturbations, with respect to the satellite track, which is almost parallel to the dawn-dusk meridian. Thus, for B_y positive the flow perturbations in the dusk sector, where the background convection cell is almost circular, are aligned more parallel to the satellite track and the cross-track component of the flow used to recognize them is reduced. In this case the detection threshold of 300 m/s is more representative of flow perturbations with higher speed. To illustrate the impact of this selection threshold, Figure 9 shows the occurrence frequency for perturbations with speeds between 100 and 300 m/s. Under these conditions the occurrence frequency maximizes in the duskside sunward background flow region for both polarities of B_y (top row in Figure 9) but increases in the duskside, where it may rise above 20% when B_y is positive (top right). This is an observational attribute that cannot be explained by the expected reorientation of the underlying large-scale convection pattern. Notice that in the region of antisunward background flow, the occurrence probabilities are always lower than those found in the region of sunward background flow but show an increase in the dawnside when B_y is positive.

5. Discussions

This work examines the mesoscale signatures embedded in the large-scale high-latitude ionospheric convection pattern at altitudes near 800 km during the summer months from the DMSP satellite F17. The measurements are taken when the thermal ion density is usually in excess of 10^5 cm^{-3} and very low noise signals from the instrumentation are obtained. The underlying large-scale convection pattern is described by attenuating discrete features with scale sizes less than 600 km. Such a description accommodates large changes in the gradient scale of the ion drift across the auroral zone and may represent significant variations from descriptions of the electric potential in an empirical model (cf. Weimer, 2001). Discrete features are isolated in the convection pattern with scale sizes between 100 and 500 km that display a local extremum in the flow. Thus, the perturbations we identify do not result from the inability of the filtering process to accommodate a large-scale gradient in the background convection. The maximum number of flow perturbations is seen at the smallest resolvable scale size, but the maximum flow speeds in a perturbation occur at scales between 200 and 400 km, where perturbation flow speeds as large as 900 m/s are observed.

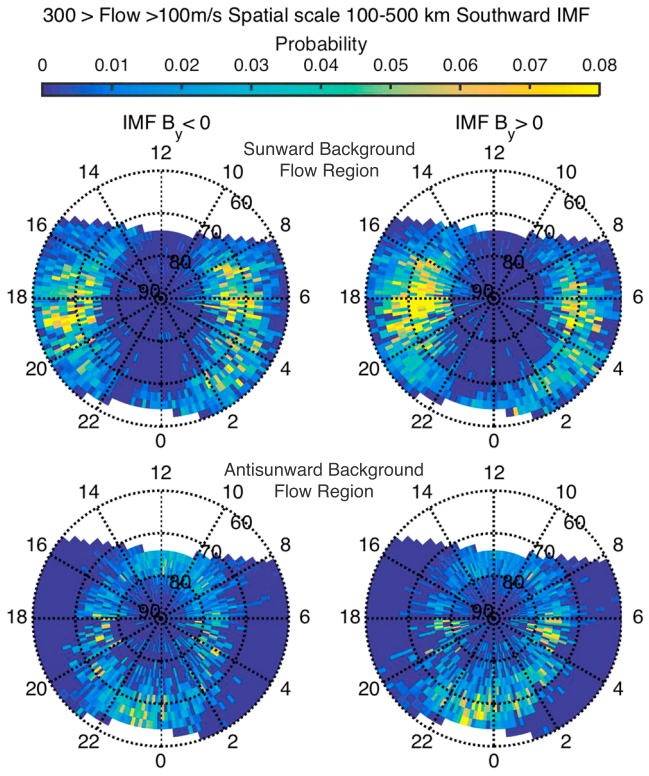

Figure 9. The occurrence probability for flow perturbations with speed between 100 and 300 m/s in the region of sunward background flows (top row) and the region of antisunward background flows (bottom row) for negative IMF B_y (left column) and positive IMF B_y (right column). IMF = interplanetary magnetic field.

Perturbation flow speeds are almost independent of the underlying convection speed in which they are embedded except for sunward directed perturbations in the dawnside embedded in sunward background flow and, though not illustrated here, are weakly dependent on the spatial gradient in the underlying flow as has been previously reported in other studies (Johnson & Heelis, 2005). During periods of southward IMF, perturbations are found throughout the region of sunward background flow and just poleward of the convection reversal in a region of antisunward background flow. The highest probability of occurrence for flow perturbations in the Northern (Southern) Hemisphere is in the region of sunward background flow on the duskside when IMF B_y is positive (negative). That is, the convection cell with the most circular geometry hosts the largest number of flow perturbations.

There are many more flow perturbations in the region of sunward background flow than in the region of antisunward background flow, and perturbations with flow speeds greater than 300 m/s have a preferred direction being sunward in the sunward background flow region and antisunward in the antisunward background flow region. Accompanying antisunward flow perturbations in the sunward background flow region and sunward perturbations in the antisunward background flow region have smaller spatial scales than the dominant population. Thus, observation suggests that flow perturbations exceeding 300 m/s are closed with smaller spatial size return flows or are closed with the lower magnitude but larger spatial size return flows. In addition, the dominant flow perturbations exceeding 300 m/s may be closed with adjacent flows across the convection reversal boundary. The asymmetry in the preferred direction of the flow perturbations in excess of 300 m/s also suggests that, in the scale size range from 100 to 400 km, these flow perturbations in a given volume represent additional sources of frictional heating and momentum transfer to the thermosphere. Further studies will elucidate the temporal persistence of these features, which would determine the effectiveness of these sources. Considering flow perturbations over the same scale size regime but with speeds between 100 and 300 m/s, we find significantly less asymmetry in the direction of the flow. Thus, while these features are efficient sources of frictional heating, they will be less efficient for momentum transfer to the neutral gas.

In this analysis we have not characterized each flow perturbation by a fraction of the underlying large-scale convection speed, but it is generally true that in the sunlit conditions considered here, except for those perturbations that span the convection reversal boundary, the remaining flow perturbations are embedded in higher-speed background flows. Thus, near the convection reversal boundary, the flow perturbations represent a region of locally intense vortical flow and in the regions of sunward background flow, the flow perturbations represent local constrictions in the more uniform flow described by the background. These features are 1° to 2° wide (~200 km) in latitude and near dawn and dusk may map to displacements in the equatorial plane of about 1 Re in the dawn-dusk dimension but in excess of 3 Re along the tail (Tsyganenko & Sitnov, 2007). Across the convection reversal boundary, the spatial scales are too large to represent local vortices within the plasma sheet boundary layer. However, it is possible that individual events are attenuated and broadened by local field-aligned potential drops to produce the larger-scale flow features observed in the ionosphere (Weimer et al., 1985). In the region of sunward background flow, the perturbation flow speeds are typically much smaller and occur over a wider range of local times than those characterized as bursty bulk flows in the magnetosphere (Angelopoulos et al., 1992, 1994), which may represent a small subset of the flow perturbations described here. Those flow perturbations occurring across the dayside are also smaller in magnitude than the flow perturbations associated with sporadic merging events described by Carlson et al. (2006). However, the spatial scale is typically the same and thus the flow perturbations described here may again represent less dramatic signatures of the same phenomenon.

The flow perturbations described here can, in principle, be represented discretely in models of the coupled ionosphere and thermosphere with the appropriate spatial and temporal resolution. The analysis

procedures undertaken here provide reasonable estimates of the scale size of events in latitude but incomplete insights into the extent of any given flow perturbation in local time (or equivalently longitude). Further analysis is required to describe the single cell or two-cell configurations that describe the flow perturbation and the accompanying closure flows required in the ionosphere. Finally, we point out that these flow perturbations are necessarily accompanied by field-aligned current distributions and accompanying energetic particle precipitation that more completely define the energy inputs to the ionosphere from the magnetosphere and the effective area over which they are delivered. Further work on this data set will allow any systematic links between these energy inputs to be described in more detail.

6. Summary

A systematic study of high-latitude ionospheric flow perturbations at mesoscale size between 100 and 500 km was conducted by analyzing ion drift measurements from the DMSP F17 during the summer months in 2012. Discrete flow perturbations that are identified are not simply due to the difference between large-scale gradients in the original signal and the filtered signal representing the background flow. The location of flow perturbations is concentrated inside and just poleward of the region with sunward background convective flow for southward IMF while more distributed at higher latitudes for northward IMF.

During times of southward IMF, there are many more flow perturbations embedded in sunward background flow than antisunward background flow. There is an asymmetry in the preferred perturbation flow direction between region of sunward and antisunward background flow, and an asymmetry in the scale size between the sunward and antisunward directed perturbations with speeds exceeding 300 m/s. However, for flow perturbations with speeds between 100 and 300 m/s significantly less asymmetry in the direction of the flow perturbation is seen. Many flow perturbations exceeding 300 m/s must be closed locally with lower magnitude return flows. This suggests that these mesoscale flow perturbations in excess of 300 m/s are additional sources of frictional heating and momentum transfer to the thermosphere.

The perturbation flow speeds are found to be almost independent of scale size and the background convection flow speed in which they are embedded, but the largest speeds are preferentially seen at scale sizes between 200 and 300 km. Maps of occurrence frequency for perturbation flow speeds above and below 300 m/s show that the highest probability of occurrence for flow perturbations is on the duskside (dawnside) in the region of sunward background flow for positive IMF B_y in the Northern (Southern) Hemisphere. Thus, the convection cell with the most circular geometry has the largest number of flow perturbations.

Acknowledgments
This work is supported by AFOSR MURI grant FA9559-16-1-0364. The interplanetary magnetic field data are available via the Space Physics Data Facility OMNIWeb interface. The link to this database is http://omniweb.gsfc.nasa.gov. The DMSP ion drift data were obtained from the William B. Hanson Center for Space Sciences at the University of Texas at Dallas. The data before 2005 are available at http://cindispace.utdallas.edu/DMSP/dmsp_data_at_utdallas.html, and the data after 2005 can be requested from Marc Hairston (hairston@utdallas.edu). The authors thank Robin Coley, Marc Hairston, and Bob Power for its use.

References

Angelopoulos, V., Baumjohann, W., Kennel, C. F., Coroniti, F. V., Kivelson, M. G., Pellat, R., et al. (1992). Bursty bulk flows in the inner central plasma sheet. *Journal of Geophysical Research*, *97*(A4), 4027–4039. https://doi.org/10.1029/91JA02701

Angelopoulos, V., Kennel, C. F., Coroniti, F. V., Pellat, R., Kivelson, M. G., Walker, R. J., et al. (1994). Statistical characteristics of bursty bulk flow events. *Journal of Geophysical Research*, *99*(A11), 21,257–21,280. https://doi.org/10.1029/94JA01263

Carlson, H. C., Moen, J., Oksavik, K., Nielsen, C. P., McCrea, I. W., Pedersen, T. R., & Gallop, P. (2006). Direct observations of injection events of subauroral plasma into the polar cap. *Geophysical Research Letters*, *33*, L05103. https://doi.org/10.1029/2005GL025230

Chen, Y.-J., & Heelis, R. A. (2018). Motions of the convection reversal boundary and local plasma in the high-latitude ionosphere. *Journal of Geophysical Research: Space Physics*, *123*, 2953–2963. https://doi.org/10.1002/2017JA024934

Chen, Y.-J., Heelis, R. A., & Cumnock, J. A. (2015). Response of the ionospheric convection reversal boundary at high latitudes to changes in the interplanetary magnetic field. *Journal of Geophysical Research: Space Physics*, *120*, 5022–5034. https://doi.org/10.1002/2015JA021024

Chen, Y.-J., Heelis, R. A., & Cumnock, J. A. (2016). Plasma and convection reversal boundary motions in the high-latitude ionosphere. *Journal of Geophysical Research: Space Physics*, *121*, 5752–5763. https://doi.org/10.1002/2016JA022796

Codrescu, M. V., Fuller-Rowell, T. J., & Foster, J. C. (1995). On the importance of E-field variability for Joule heating in the high-latitude thermosphere. *Geophysical Research Letters*, *22*(17), 2393–2396. https://doi.org/10.1029/95GL01909

Codrescu, M. V., Fuller-Rowell, T. J., Foster, J. C., Holt, J. M., & Cariglia, S. J. (2000). Electric field variability associated with the Millstone Hill electric field model. *Journal of Geophysical Research*, *105*(A3), 5265–5273. https://doi.org/10.1029/1999JA900463

Cosgrove, R. B., & Codrescu, M. (2009). Electric field variability and model uncertainty: A classification of source terms in estimating the squared electric field from an electric field model. *Journal of Geophysical Research*, *114*, A06301. https://doi.org/10.1029/2008JA013929

Cousins, E. D. P., & Shepherd, S. G. (2010). A dynamical model of high-latitude convection derived from SuperDARN plasma drift measurements. *Journal of Geophysical Research*, *115*, A12329. https://doi.org/10.1029/2010JA016017

Cousins, E. D. P., & Shepherd, S. G. (2012). Statistical maps of small-scale electric field variability in the high latitude ionosphere. *Journal of Geophysical Research*, *117*, A12304. https://doi.org/10.1029/2012JA017929

Crowley, G., & Hackert, C. L. (2001). Quantification of high latitude electric field variability. *Geophysical Research Letters*, *28*(14), 2783–2786. https://doi.org/10.1029/2000GL012624

Deng, Y., Maute, A., Richmond, A. D., & Roble, R. G. (2009). Impact of electric field variability on Joule heating and thermospheric temperature and density. *Geophysical Research Letters*, *36*, L08105. https://doi.org/10.1029/2008GL036916

Deng, Y., & Ridley, A. J. (2007). Possible reasons for underestimating Joule heating in global models: *E* field variability, spatial resolution, and vertical velocity. *Journal of Geophysical Research*, *112*, A09308. https://doi.org/10.1029/2006JA012006

Dungey, J. W. (1961). Interplanetary magnetic field and the auroral zones. *Physical Review Letters*, *6*(2), 47–48. https://doi.org/10.1103/PhysRevLett.6.47

Fuller-Rowell, T. J., Rees, D., Quegan, S., Mo•ett, R. J., Codrescu, M. V., & Millward, G. H. (1996). A coupled thermosphere-ionosphere model; CTIM). In Ed. R. W. Schunk (Ed.), *STEP Handbook of ionospheric models* (pp. 217–238). Logan, Utah: Utah State University.

Gabrielse, C., Nishimura, Y., Lyons, L., Gallardo-Lacourt, B., Deng, Y., & Donovan, E. (2018). Statistical properties of mesoscale plasma flows in the nightside high-latitude ionosphere. *Journal of Geophysical Research: Space Physics*, *123*. https://doi.org/10.1029/2018JA025440

Hairston, M. R., & Heelis, R. A. (1995). Response time of the polar ionospheric convection pattern to changes in the north-south direction of the IMF. *Geophysical Research Letters*, *22*(5), 631–634. https://doi.org/10.1029/94GL03385

Johnson, E. S., & Heelis, R. A. (2005). Characteristics of ion velocity structure at high latitudes during steady southward interplanetary magnetic field conditions. *Journal of Geophysical Research*, *110*, A12301. https://doi.org/10.1029/2005JA011130

Kivanç, Ö., & Heelis, R. A. (1998). Spatial distribution of ionospheric plasma and field structures in the high-latitude *F* region. *Journal of Geophysical Research*, *103*(A4), 6955–6968. https://doi.org/10.1029/97JA03237

Lu, G., Emery, B. A., Rodger, A. S., Lester, M., Taylor, J. R., Evans, D. S., et al. (1996). High-latitude ionospheric electrodynamics as determined by the assimilative mapping of ionospheric electrodynamics procedure for the conjunctive SUNDIAL/ATLAS 1/GEM period of March 28–29, 1992. *Journal of Geophysical Research*, *101*(A12), 26,697–26,718. https://doi.org/10.1029/96JA00513

Lyons, L. R., Nishimura, Y., Kim, H.-J., Donovan, E., Angelopoulos, V., Sofko, G., et al. (2011). Possible connection of polar cap flows to pre- and post-substorm onset PBIs and streamers. *Journal of Geophysical Research*, *116*, A12225. https://doi.org/10.1029/2011JA016850

Matsuo, T., & Richmond, A. D. (2008). Effects of high-latitude ionospheric electric field variability on global thermospheric Joule heating and mechanical energy transfer rate. *Journal of Geophysical Research*, *113*, A07309. https://doi.org/10.1029/2007JA012993

Matsuo, T., Richmond, A. D., & Hensel, K. (2003). High-latitude ionospheric electric field variability and electric potential derived from DE-2 plasma drift measurements: Dependence on IMF and dipole tilt. *Journal of Geophysical Research*, *108*(A1), 1005. https://doi.org/10.1029/2002JA009429

Milan, S. E., Lester, M., Cowley, S. W. H., & Brittnacher, M. (2000). Convection and auroral response to a southward turning of the IMF: Polar UVI, CUTLASS, and IMAGE signatures of transient magnetic flux transfer at the magnetopause. *Journal of Geophysical Research*, *105*(A7), 15,741–15,755. https://doi.org/10.1029/2000JA900022

Pinnock, M., Rodger, A. S., Dudeney, J. R., Baker, K. B., Newell, P. T., Greenwald, R. A., & Greenspan, M. E. (1993). Observations of an enhanced convection channel in the cusp ionosphere. *Journal of Geophysical Research*, *98*(A3), 3767–3776. https://doi.org/10.1029/92JA01382

Reiff, P. H., & Burch, J. L. (1985). IMF B_y-dependent plasma flow and Birkeland currents in the dayside magnetosphere: 2. A global model for northward and southward IMF. *Journal of Geophysical Research*, *90*(A2), 1595–1609. https://doi.org/10.1029/JA090iA02p01595

Richmond, A. D., & Kamide, Y. (1988). Mapping electrodynamic features of the high-latitude ionosphere from localized observations: Technique. *Journal of Geophysical Research*, *93*(A6), 5741–5759. https://doi.org/10.1029/JA093iA06p05741

Richmond, A. D., Ridley, E. C., & Roble, R. G. (1992). A thermosphere/ionosphere general circulation model with coupled electrodynamics. *Geophysical Research Letters*, *19*(6), 601–604. https://doi.org/10.1029/92GL00401

Ridley, A. J., Lu, G., Clauer, C. R., & Papitashvili, V. O. (1998). A statistical study of the ionospheric convection response to changing interplanetary magnetic field conditions using the assimilative mapping of ionospheric electrodynamics technique. *Journal of Geophysical Research*, *103*(A3), 4023–4039. https://doi.org/10.1029/97JA03328

Roble, R. G., & Ridley, E. C. (1994). A thermosphere-ionosphere-mesosphere-electrodynamics general circulation model (TIME-GCM): Equinox solar cycle minimum simulations (30–500 km). *Geophysical Research Letters*, *21*(6), 417–420. https://doi.org/10.1029/93GL03391

Ruohoniemi, J. M., & Baker, K. B. (1998). Large-scale imaging of high-latitude convection with Super Dual Auroral Radar Network HF radar observations. *Journal of Geophysical Research*, *103*(A9), 20,797–20,811. https://doi.org/10.1029/98JA01288

Shepherd, S. G., Ruohoniemi, J. M., & Greenwald, R. A. (2003). Direct measurements of the ionospheric convection variability near the cusp/throat. *Geophysical Research Letters*, *30*(21), 2109. https://doi.org/10.1029/2003GL017668,%2021

Tsyganenko, N. A., & Sitnov, M. I. (2007). Magnetospheric configurations from a high-resolution data-based magnetic field model. *Journal of Geophysical Research*, *112*, A06225. https://doi.org/10.1029/2007JA012260

Weimer, D. R. (2001). An improved model of ionospheric electric potentials including substorm perturbations and application to the Geospace Environment Modeling November 24, 1996, event. *Journal of Geophysical Research*, *106*, 407–416. https://doi.org/10.1029/2000JA000604

Weimer, D. R., Goertz, C. K., Gurnett, D. A., Maynard, N. C., & Burch, J. L. (1985). Auroral zone electric fields from DE 1 and 2 at magnetic conjunctions. *Journal of Geophysical Research*, *90*(A8), 7479–7494. https://doi.org/10.1029/JA090iA08p07479

Wild, J. A., & Yeoman, T. K. (2000). CUTLASS HF radar observations of high-latitude azimuthally propagating vortical currents in the nightside ionosphere during magnetospheric substorms. *Annales de Geophysique*, *18*(6), 640–652. https://doi.org/10.1007/s00585-000-0640-7

Yu, Y., & Ridley, A. J. (2009). Response of the magnetosphere-ionosphere system to a sudden southward turning of interplanetary magnetic field. *Journal of Geophysical Research*, *114*, A03216. https://doi.org/10.1029/2008JA013292

Zou, Y., Nishimura, Y., Lyons, L. R., Donovan, E. F., Ruohoniemi, J. M., Nishitani, N., & McWilliams, K. A. (2014). Statistical relationships between enhanced polar cap flows and PBIs. *Journal of Geophysical Research: Space Physics*, *119*, 151–162. https://doi.org/10.1002/2013JA019269